Rietveld Texture Analysis from Synchrotron Diffraction Images: II. Complex multiphase materials and diamond anvil cell experiments

Hans-Rudolf Wenk[1)], Luca Lutterotti[2)], Pamela Kaercher[1)], Waruntorn Kanitpanyacharoen[1)], Lowell Miyagi[3)], Roman Vasin[1,4)]

Department of Earth and Planetary Science, University of California, Berkeley, CA
Department of Industrial Engineering, University of Trento, Italy
Department of Geology and Geophysics, University of Utah, Salt Lake City
Frank Laboratory of Neutron Physics, Joint Institute for Nuclear Research, Dubna, Russia

Abstract

Synchrotron X-ray diffraction images are increasingly used to characterize crystallographic preferred orientation distributions (texture) of fine-grained polyphase materials. Diffraction images can be analyzed quantitatively with the Rietveld method as implemented in the software package MAUD (Materials Analysis Using Diffraction). Here we describe the analysis procedure for diffraction images collected with high energy X-rays for a complex, multiphase shale, and for those collected *in situ* in diamond anvil cells at high pressure and anisotropic stress.

Key words: Texture analysis, Synchrotron diffraction, Rietveld method, Shale, Diamond anvil cell

I. INTRODUCTION

In a companion paper (Lutterotti *et al*., 2013), we have described the basic steps for texture analysis from synchrotron diffraction images with the Rietveld method, using the software MAUD (Lutterotti *et al*., 1997). We assume that the reader is familiar with the introductory paper. Here we discuss complexities which arise for samples with many phases and samples which are highly deformed.

The first example is a sedimentary shale composed of multiple types of minerals, with different volume fractions, microstructures, and orientation distributions (OD). The second complex sample is magnesiowuestite (Mg,Fe)O, measured *in situ* at ultrahigh pressure and anisotropic stress conditions in a diamond anvil cell (DAC). Keep in mind that we provide only an outline of analysis procedures. The Rietveld method and its implementation in MAUD is very general and lends itself to many applications, each of which may require slightly different approaches, modifications, and application of specific models. With the two examples we try to introduce several of the capabilities of MAUD which a user may consider for a particular sample, including sample rotations, background models and symmetry transformations. Step by step guides are provided as two appendices. Together with data files they can be freely downloaded from the internet (http://PD-journal.htm). We refer to corresponding sections in the introductory paper (Lutterotti et al. 2013) as e..g. "Part I, step 4".

II. SHALE AS AN EXAMPLE OF A COMPLEX POLYPHASE MATERIAL

A. Diffraction experiment

Shale is a sedimentary rock and composed of a wide variety of minerals. Sheet silicates comprise a large volume fraction of shales and align preferentially parallel to the bedding plane during sedimentation and compaction. Crystallographic preferred orientation (CPO) of phyllosilicates is of great interest, because it is the primary cause of elastic anisotropy observed during seismic prospecting of oil and gas deposits. Thus several studies have focused on improving synchrotron X-ray techniques to quantify textures and microstructures of shales (*e.g.*, Wenk *et al.*, 2008; Lutterotti *et al.*, 2010; Kanitpanyacharoen *et al.*, 2011, 2012; Vasin *et al*., 2013).

For this tutorial we use a sample of Kimmeridge shale from the North Sea, UK (Hornby, 1998; Vasin *et al*., 2013). The sample is a slab, 2mm thick (Figure 1a). It was measured at the

APS high energy beamline ID-11C during the same session as the nickel coin (Lutterotti *et al.*, 2013) and therefore the same instrument parameters can be applied which were obtained by refining the CeO_2 standard (see Part I.III). The wavelength was 0.10798 Å, and the beam size 0.5×0.5 mm. During X-ray exposure the sample was translated along the horizontal axis from –2.5 to +2.5 mm to increase the measured volume, and rotated around the *É*-axis Y_M (Figure 1 in Lutterotti *et al.*, 2013), from –45° to +45° in 15° increments (i.e., there are 7 diffraction images) to obtain adequate pole figure coverage (Figure 1b).

Images were collected with a Perkin Elmer amorphous silicon detector with dimensions of 2048×2048 pixels and a pixel size of 200×200 µm. The detector was approximately 1850 mm from the sample. Figure 2a shows a diffraction image with many Debye-rings from at least six major phases. Several rings display strong intensity variations due to preferred orientation.

B. Preliminary analysis for axial symmetry using one image

Refining seven images simultaneously with a number of low-symmetry phases is time-consuming (2D diffraction images are integrated in angular azimuthal increments, resulting in a total of several hundred patterns). Thus it is more efficient to start with only one image measured at *É* = 0° (coverage in Figure 1b). Later we will add the other images in different datasets to complete the analysis (coverage in Figure 1c). The procedure with a single image is justified, because shale textures have approximately axial (fiber) symmetry about the bedding plane normal (transverse isotropy). By imposing this sample symmetry, complete pole figure coverage is obtained with only one dataset. If the texture is not too strong, one can initially assume a random orientation to simplify the first refinement steps and introduce the texture later with the additional images. In case of a very strong texture we have to work from the start with all images and a complete texture model, but this is not the case for the shale example.

We start from an instrument calibrated with the CeO_2 standard and use the same procedure as for the coin analysis (Part I.IV) to load and integrate the first image. ???But compared to the coin we do not rotate the image 90˚ counterclockwise before processing, as for the shale sample we have already the bedding plane in the center of the pole figure (see Figure 1b and c). Since the texture of shale is smoother than the coin (see Figure 2a) and we can employ a larger integration step of 10˚. This reduces the total amount of data to analyze without loosing information and speeds up the computation. Initially we restrict the refinement range to 2¸ = 0.3

– 3.0° since shale contains several low-symmetry phases with many diffraction peaks that overlap at higher 2¸ those peaks do not provide much information for texture analysis. Restricting the range greatly speeds up the computation. If necessary the range can be enlarged at the end of the refinement.

Figure 3 (bottom) displays the stack of experimental diffraction patterns taken at each 10° increment in eta. The pole figure coverage is shown in Figure 1b with the pole to the bedding plane at A (*É* rotation axis).

We use a 4th order polynomial background common to all patterns (5 coefficients), however we must also correct for small angle scattering from platelet-shaped phyllosilicate nanoparticles, which is best visible in the diffraction image at very low angles (2θ H0.1-0.2°), near the beamstop (Figure 2a). Since these platelets are oriented, also small angle scattering displays azimuthal intensity variations. The broad low angle peak extends as elevated background to the first diffraction peaks of phyllosilicates (2¸ H0.3-0.6°) (Figure 3). To fit this peak we use two symmetrical background peaks which are are Pseudo-Voigt functions that can be positioned arbitrarily in a dataset at any coordinates. The principal one is 2θ (parameters are intensity, 2θ position, half width at half maximum HWHM in 2θ, and the Gaussian content), but it may span over η (adding a position, HWHM and Gaussian content in η) as well as position angles (χ, ϕ). Background peaks are useful to model some well-defined bumps occurring in images that do not belong to diffraction from a phase. For details see the tutorial in Appendix 1.

We limit the refinement to the five major phases: quartz, pyrite, kaolinite, illite-mica, and illite-smectite. There are minor phases such as feldspars with less than 5% volume and no significant texture. Quartz and pyrite structures can be found in the Crystallography Open Database (Gražulis et al., 2009) or on the small database included with MAUD (structures.mdb). We added the following structures: triclinic kaolinite (Bish and Von Dreele, 1989), monoclinic illite-mica (Gualtieri, 2000), and monoclinic illite-smectite (Plançon *et al.*, 1985). The corresponding Crystallographic Information Files (.cif) are available in the on-line material supplied with the tutorial. For monoclinic phases the first monoclinic setting has to be used to work with texture (Matthies and Wenk, 2009). All texture models implemented in MAUD have been written for the monoclinic "*c*" setting (i.e. $\alpha = \beta = 90°$ and $\gamma \neq 90°$); otherwise crystal symmetries are not imposed correctly, including the orientation distribution integration paths. It means that the angle different from 90˚ is γ. In MAUD one can change from one setting to

another simply by editing the phase and in the General tab, selecting the desired setting in the Space Group drop-down list. Lattice parameters and atomic positions are adjusted automatically, for example, for the illite-mica phase changing from C2/c:b1 to C2/c:c1 makes *c* the unique (2-fold) axis. The "1" at the end of the space group symbol stands for first origin and the setting letter is after the colon. The provided .cif file for illite-smectite is already in the first (c) setting.

When multiple phases are entered, MAUD automatically assigns to each phase the same volume fraction. In Rietveld programs, each phase has an assigned scale factor, and each scale factor is optimized during the refinement. Then from the refined scale factors, the volume and weight fractions of the phases are computed. In addidtion to volume fraction, the scale factor contains information about the beam intensity and other factors such as absorption, yet is treated as a unique parameter. In the case of texture we need an approach that models the sample correctly and uses phase fractions, beam intensities, layer thicknesses and absorption corrections (Lutterotti, 2010) which all contribute to peak intensities and thus may complicate intensity. In our final model, dealing with seven images, we will have a beam intensity parameter for each image, all patterns in one image will share the same beam intensity, and then we refine the phase fractions for all phases minus one (MAUD imposes that the sum of all phase fractions need to be equal to 1, and enforces the unrefined phase to be the complement to 1).

With a complex sample like this shale, it is important to provide reasonable initial estimates of phase volume fractions.. This saves avoids divergence of the solution in the initial steps of the least squares algorithm. Weight fractions are calculated automatically by MAUD using the provided atomic structure and unit cell parameters.

For the texture, with the initial simplified model using only one image, we need to impose the axial symmetry that in MAUD is always imposed around the center of the pole figure (Figure 1b and c; for the MAUD angle convention and transformations see Grässlin et al., 2013 and Figure 4a in Part I). [Luca modify!]

After manually adjusting some parameters such as unit cell parameters, beam intensity and background to better fit the experimental patterns (in the parameter list on the MAUD main page, column “Value”) we start with the refinement of some basic parameters. In the Rietveld refinement procedure it is always better to avoid refining too many parameters at the beginning and to “guide” the program to the solution. There are normally three major steps to follow: 1) refine background parameters and intensities (scale factors or in MAUD beam intensities and

phase fractions), 2) refinement parameters connected to the peak positions (unit cell parameters and 2θ errors), 3) refine microstructural parameters such as crystallite sizes and microstrain. While doing subsequent refinements, keep the previous parameters set to refine. When do we refine texture-related parameters? If the texture is smooth, or weak, it is done at the end (a fourth step) to avoid refining texture instead of some other parameter that could impose intensity variations (e.g. absorption). But if the texture is sufficiently strong we introduce the texture refinement along with the refinement of intensities in the second step, as long as diffraction peak positions are well-constrained. The crystal structure (e.g. atomic positions and even lattice parameters) should be refined only if necessary and for well-defined phases. Also, use only one overall B factor (temperature factor) by clicking on "Bound B factor" in the parameter list. When working at high energy X-rays and very low 2θ angles (angle span is short) the data are insensitive to B factors. As in the case of the coin in Part I, we should refine the *x* and *y* image centering errors as we cannot assure that the CeO_2 calibrant was in the center of the beam, whereas for the shale the beam is inside the sample.

Looking at Figure 3, diffraction peaks of kaolinite (K), illite-mica (IM), and illite-smectite (IS) show strong η-dependent intensity variations indicative of texture. The intensities of the quartz (Q) and pyrite (P) diffraction peaks are almost constant, except for several increased intensity spots due to scattering from larger grains (e.g. P 111). Thus we only refined preferred orientations of the three phyllosilicates but not for quartz and pyrite. We used the EWIMV model (Part I-IV) for the kaolinite and the illite-mica with a large orientation distribution cell size of 10˚ given the smooth character of the texture. In general, do not select a smaller cell size than the measured grid in patterns (in this case 10˚ integration sectors).

For illite-smectite, with a well-defined orientation we use the so-called standard functions method to introduce this capability (Matthies et al., 1987 and implemented in MAUD by Lutterotti et al., 2007). The advantage of this approach is that we can use some texture-like functions with only few parameters. MAUD implements Gaussian or Lorentzian fiber components (having a fiber symmetry character) and spherical components (also Gaussian, Lorentzian or mixed). For both types of components we refine position, spread (in degrees) and Gaussian or Lorentzian character (one mixing parameter). For the position, the fiber component is defined by the fiber axis orientation respect to the sample normal (azimuthal PhiY and polar angle ThetaY) and the orientation axis in the unit cell (also two angles: the azimuthal angle with

respect to the *c* axis PhiH and the polar angle starting from the *a* axis ThetaH; see for analogy the angles ϕ and β in the appendix of Popa, 1992). Standard function texture corrections are very quick to compute and converge rapidly. Another advantage of the standard functions is that they can model very smooth or very sharp textures up to epitaxial films, or even single crystal like patterns, depending on the spread parameter. We defined the fiber axis parallel to the sample normal (azimuthal and polar angles equal zero). For the crystallographic texture orientation, we know that the *h*00 maximum is in the center of the pole figure (monoclinic first setting) and we set the azimuth PhiH to 90˚ and the polar angle ThetaH to 0˚. In this case we do not refine the orientation angles as they do not deviate from the imposed starting values and only the spread and Gaussian character of the fiber component will be refined.

The illite-smectite peaks are asymmetrical (Figure 4) due to complications from turbostratic disorder which is typical of clay minerals. This kind of disorder can be described with the Ufer single layer model (Ufer et al., 2004). The model is very effective in reproducing the asymmetric broadening caused by the turbostratic disorder and can be coupled with the texture analysis (Lutterotti et al., 2010). We only need to define the faulting direction (*h*00) for the smectite and the supercell dimension, to approximate the disordered structure. We choose 10 times the *a* axis (first setting) as a sufficient value to model the disorder.

In Figure 3 (top) we can see the resulting 2D plot after the initial refinement with one image and the agreement with the experiment is very good (Figure 3, bottom). Figure 4 shows two individual patterns, one with scattering vectors parallel to and the other to perpendicular to the bedding plane normal and also here good agreement for both is observed. The tickmarks at the bottom denote peaks belonging to each phase. Table I lists refined volume and weight fractions for the phases and Table II gives information about the texture. Corresponding pole figures are shown in Figure 5a in equal area projection. Note that illite-mica has the sharpest texture and illite-smectite shows the broadest distribution. The R-factors which indicate the overall goodness of fit between the model and experimental data for the single image refinement were: R_w = 12.5% and R_b = 8.9%. In general, R-factors smaller than 15% demonstrate a very good refinement.

C. Analysis without imposing texture symmetry

With this preliminary refinement, we can add the other six diffraction images and proceed with the full analysis. In the end we can also enlarge the refinement range.

With all the 7 images rotated in 15 increments around ω and integrated in 10˚ sectors around η, the pole figure coverage is now as shown in Figure 1c. [Luca modify] After the 90° χ rotation of the sample coordinate system, the pole to the bedding plane is in the center (Figure 1d). With the larger OD coverage we can analyse the full texture without imposing sample symmetry and use EWIMV, also for the illite-smectite. In EWIMV the default in MAUD is to use all the reflections in the computing range. Contrary to the classical WIMV and pole figures texture analysis, in Rietveld-EWIMV the pole figure value is weighted using the square root of the theoretical random intensity of the reflection (equation (2) in Lutterotti et al., 2004 [added]). In this case, if we use the full range, the three textured phases have many overlapped and very weak reflections, even up to 3˚ in 2θ. Weak overlapped reflections do not contribute significantly to the OD and introduce noise. The texture analysis improves if such reflections are not used, as long as there is no problem with coverage. EWIMV and WIMV have an option to reject reflections with either small intensities relative to the strongest reflection or *d*-spacings lower than a threshold value. In the present analysis we use this option and avoided reflections smaller than 2% of the strongest reflection and with *d*-spacings smaller than 1.5 Å.

Figure 6 shows the final fit to all seven diffraction imageswith a cumulative plot of all patterns for the dataset $\omega = 0^{\circ}$ and a 2θ range 0.4-7.8˚. At low angles kaolinite, illite-mica and illite/smectite dominate, whereas at high angles quartz and pyrite dominate. In a case like this it is important to check the B factors. Wrong B factors between the pyrite/quartz and the other low angle phases may lead to angular-dependent errors that will greatly affect the phase fractions between the low angle and high angle phases.

Pole figures of phyllosilicates, corresponding to those in Figures 5a but without imposing symmetry, are shown in Figure 5b. Note that these pole figures look slightly different from what you might see in your plot in MAUD. This is because the orientation distribution data have been exported from MAUD and were replotted in the software BEARTEX (Wenk et al., 1998) in order to plot the pole figures on the same scale. The new pole figures show minor deviations from axial symmetry, particularly an elongation of the pole figure maximum in the vertical direction for (001) in kaolinite and (100) in illite-mica and illite-smectite. Comparing this with

the coverage (Figure 1d), we note that this distortion extends into the blind region and may be an artifact. This is further supported by the fact that maximum pole densities are higher if axial symmetry is imposed (Table II). Only additional measurements with rotations around other sample axes could verify if the preferred orientation pattern has perfect axial symmetry. In Figure 7 we also show pole figures (100) of kaolinite and (010) of illite-mica and illite-smectite that display a peripheral circle and it is again questionable if pole density variations along this girdle are real.

In this tutorial presentation we have started with a single image and imposed axial symmetry, then progressed to many images with no symmetry. This was done to progress from a simple to a more complex analysis. In reality one may want to progress the opposite way: first, with many images, verify sample symmetry; second perform necessary sample rotations to bring sample symmetry axes to coincidence with MAUD coordinates, and finally impose symmetry with one image (for axial symmetry) or several images for more complex sample symmetries.

Another issue is coverage. Shales have very special textures with a maximum of platelet normals perpendicular to the bedding plane (Figure 5). This maximum has been well sampled with the present coverage (Fig. 1d), however directions in the platelet plane have minimal coverage (Figure 7). To assess this it would be advantageous not to rotate the sample about the pole to the bedding plane (Figure 1a, c) or to combine measurements from different sample directions as mentioned above. Such issues should be considered for each particular case.

Phase volume fractions for Kimmeridge shale without imposing sample symmetry are compared in Table I with results for axial symmetry. They are very similar. For the Kimmeridge shale the final Rietveld R_w factor is 10.9% (R_b = 8.2%) for the refinement in the 2¸ range up to 3˚. A few peaks are missing from the calculated diffraction pattern, some are too intense, and some have wrong shapes (*e.g.*, Figs. 3, 4). The missing peaks are mostly due to feldspar that could be entered into the refinement. Anisotropic crystallite shapes and microstrains could also be imposed for phyllosilicates. We have used a CeO_2 powder to refine instrumental parameters (Part I), but CeO_2has no diffraction peaks at 2¸ < 2°. Thus the function describing the instrumental part of diffraction peak broadening (especially the asymmetry) is poorly constrained for this shale with diffraction peaks down to 2¸ H0.5°. Parts of the instrumental peak shape function (the asymmetry) can be refined as has been done for the full range analysis (see Figure 6). The final R_w for the refinement of the full range and all seven images was reduced from the

one image refinement to 10.3% (R_b = 7.4%) which is a very good value, given the number of patterns and complexity of the phases.

III. DIAMOND ANVIL CELL IN RADIAL DIFFRACTION GEOMETRY

A. Experiment

Rietveld texture analysis of synchrotron diffraction images can be applied to study *in situ* deformation at high pressures with a diamond anvil cell in radial diffraction geometry (rDAC) (*e.g.*, Wenk *et al*., 2006). This proves to be an important method to determine deformation mechanisms at ultrahigh pressures, as in the deep earth (*e.g.*, Miyagi *et al*., 2010) to explain observed seismic anisotropy in the lower mantle and inner core, and to study crystal orientation changes during phase transformations (e.g. Miyagi *et al*., 2008; Kanitpanyacharoen *et al*., 2012b, Kaercher et al. 2012). The method can also be applied to analyze data from multi-anvil experiments such as D-DIA (*e.g.*, Wenk *et al*., 2005, 2013).

The geometry of a typical rDAC deformation experiment is shown in Figure 8a,b. Diamonds not only impose pressure but also differential stress that deforms crystals in the aggregate. The diamond cell is set up in radial rather than axial geometry, i.e. the X-ray beam passes through the sample perpendicular to the compression direction so that the diffraction image records reflections from lattice planes oriented from parallel to perpendicular to compression (Figure 2c). Preferred orientation is expressed in the azimuthal intensity variations, similar to the images of the shale (Figure 2a).

rDAC experiments have been performed at room temperature to pressures as high as 200 GPa on iron (Wenk *et al*., 2000) and 185 GPa on $MgSiO_3$ post-perovskite (Miyagi *et al*., 2010). More recently texture measurements have been made in the rDAC on magnesiowuestite (Mg,Fe)O at 2273 K and H65 GPa, using a combination of resistive and laser heating (Miyagi *et al*., 2013).

Contrary to the coin and shale experiments, we must take into account changes with pressure, and particularly the macroscopic stress field which imposes anisotropic elastic distortions of the lattice. As an example we use ferropericlase (magnesiowuestite) which has been previously investigated with rDAC experiments (*e.g.*, Merkel *et al*. 2002; Kunz *et al*., 2007; Lin *et al*., 2009; Kaercher *et al*., 2012). This particular sample $(Mg_{0.75}Fe_{0.25})O$ has been described by Kunz et al. (2007).

The rDAC experiment was performed at the high pressure beamline 12.2.2. of the Advanced Light Source at Lawrence Berkeley National Laboratory. Ferropericlase powder was loaded into a boron-kapton gasket. The initial sample diameter was 80 µm with a starting

thickness of 50 µm. The sample was compressed in an rDAC, using diamond anvils with 300 µm diameter culets (Fig. 8c). Diffraction images were recorded with a Mar3450 image plate detector, with dimensions of 3450×3450 and a pixel size of 100×100 µm, positioned approximately 285 mm from the sample with an X-ray wavelength of 0.49594 Å.

There are two immediate complications. First, the beam passes not just through the sample but also through a gasket, which is needed to maintain pressure. Thus there are additional diffraction lines from the gasket material, especially at low angles (Figure 2c). Gaskets for radial DAC experiments must be made of materials that scatter as little as possible. At lower pressures, amorphous boron (< 100 GPa) has been used, while at higher pressure, cubic boron nitride or beryllium have been used. For beryllium which scatters more, it is advantageous to tilt the cell to have minimum beam interference. If the cell is tilted significantly, the tilt needs to be accounted for by entering the appropriate sample rotation angles in MAUD. Bright diffraction spots from the diamond may appear in the diffraction pattern. In fact, the large spot on the left side of Figure 2c (arrow) is attributed to diamond. This effect can be minimized by slightly rotating or tilting the DAC. Intense spots can also be eliminated by image processing.

A second complication is imposed anisotropic elastic strain. Lattice plane spacings are smaller in the compression direction and larger perpendicular to the compression axis. Thus, the Debye rings are not circles but ellipses. The resulting sinusoidal variations of the diffraction peak positions with azimuthal angle are best seen in unrolled images (Fig. 9a, bottom).

B. Initial setup

Instrument calibration.

Before analyzing the MgFeO diffraction pattern, instrument parameters have to be refined with a reference sample. In this case LaB_6 was used, adopting the NIST-recommended unit-cell parameter a = 4.15689 Å (Figure 2b). As with CeO_2, the unit-cell parameter and the wavelength are kept fixed, while detector centering, tilts and distance from the sample are refined. See the Appendix 2 for a step-by-step guide for calibrating instrument parameters using the ImageJ plugin in MAUD. The MAUD procedure has been used for the detector calibration and subsequent analysis with the magnesiowuestite in order to separate the effects on the diffraction rings due to detector misalignement from the applied stresses. For the refinement of instrument parameters we did not use any asymmetry in the Caglioti parameters as the measured diffraction

peaks are far from the image center and thus do not show any broadening asymmetry. Also, in this case there is no η angle dependent broadening.

During the refinement of the standard LaB_6 we noted additional peaks due to sample contamination of which some are very small and can simply be neglected. One peak at 2¸ H 15.78° is significant and therefore we excluded the region 2¸ H15.5-16° from the analysis. A complication arises from the coarse nature of the sample with respect to the small beam size, causing some intense "spots" originating from diffraction from a few very large grains (Fig. 2b). In general it would be advisable not to use such a coarse-grained impure standard or to be able to spin the sample to avoid graininess problems. We used a so-called Le-Bail refinement (Le Bail et al., 1988) but permitting different values of the intensities/structure factors for each pattern. In MAUD a Le-Bail structure factor extraction is done with the restriction that different patterns (same instrument) share the same structure factors. Here we want to allow the variation of peak intensity with azimuthal angle. This is done in MAUD using the texture model "Arbitrary Texture", where intensity variations are neither bound to an OD, nor to a crystal structure. For the refinement of instrument parameters we did not use any asymmetry in the Caglioti parameters as the measured diffraction peaks are far from the image center and thus do not show any broadening asymmetry. Also, in this case there is no η angle dependent broadening.

Next we start processing the ferropericlase DAC image. Because of the anvil cell geometry we cannot tilt the sample, and the number of diffraction rings and their extension is limited. Since stresses are of interest and with the small angular range, it is important to have a very good detector calibration to correctly separate the detector misalignement from the stress contribution to diffraction rings becoming elliptical.

We use the instrument calibration values obtained by the LaB_6 refinement and process the DAC image as described in Part I. We integrated the image in 5° sectors to generate 72 patterns. This smaller integration step is essential in this case, because the texture is sharp and significant peak shifts occur due to anisotropic stress. If the integration step is too large, the variations of diffraction peak positions and intensities can not be accounted for properly. We choose a computation range from 6° to 24° in 2 θ in order to include the four prominent diffraction peaks (111), (200), (220) and (311) of magnesiowuestite (Figure 9) and to exclude diffractions from gasket material. In Figure 9a (bottom) there is a sharp spot at 2 θ H23.8°. This is a diffraction spot from the diamond anvil (Figure 2b, arrow). However, not being too intense

we do not need to disable this diffraction spectrum as ir does not significantly affect the refinement. In other cases, if the spots from the diamond anvils influence the results, then the spectra containing diffraction from the anvils should be disabled. A test by running refinement both including and excluding the pattern with the single crystal spot, can be done to check for its influence. Spots can also be eliminated from the diffraction images by processing (e.g. in ImageJ).

The waviness of the lines (Figure 9a, bottom) is not due to a centering or tilting error of the detector, but to the deviatoric part of the applied stress, i.e. the difference between the compression along the main compression axis of the anvil cell (indicated by arrow: large 2θ, small d) and the transverse direction.

Setting up the background in rDAC experiments can be difficult due to scattering and absorption from gaskets and DAC absorption effects (Fig. 2c). In this case it is best to use an interpolated background (independent for each pattern). A first positioning of interpolation points is done automatically using an algorithm described by Sonneveld and Visser (1975) and selecting only the starting interval between points and the number of iterations of the algorithm optimizing the position. After the automatic positioning by the routine, the number and positions of the points can be adjusted manually but in the case of many patterns this may be time consuming as it should be done pattern by pattern. The use of the algorithm and the presence of patterns with different angular ranges causes a possibility of a different choice of interpolation points for each pattern). A perfect position of the interpolation points is not so critical in MAUD because the interpolation is performed not on the raw experimental data, but on the residual after the intensity diffracted by all phases has been calculated and subtracted from the experimental pattern. Nevertheless, it is advantageous not to have interpolation points at positions of strong reflections.

For the refinement we used a periclase phase (MgO, cubic, Fm-3m) and substitute 25% Fe substituting for Mg to reach the ferropericlase composition. The calculated pattern (Figure 9a, top) differs significantly from the experimental DAC patterns (Figure 9a, bottom). This is due to the high pressure condition (43.9 GPa) that shrinks the cell (a) and enlarges 2θ. Thus the lattice parameter has to be adjusted manually.

With only one image and four diffraction peaks, the coverage is largely insufficient to refine the OD without imposing sample symmetry. But in this DAC experiment texture should

have axial symmetry around the compression direction. Before imposing axial symmetry we have to make sure that the compression direction (symmetry axis) is indeed in the center of the MAUD pole figure. We set the Z_M axis of our sample coincident with the compression axis by setting the χ value to 90° (Part I, Figure 3 for the MAUD angle conventions and Grässlin et al., 2013). The coverage (after this rotation) is shown in Figure 8d.

C. Stress models

Macrostress. Lattice strain is due to the imposed anisotropic elastic stress and the elastic properties of the crystal. It is exhibited as sinusoidal oscillations in peak position with azimuth (Figure 9b, bottom).

There are four models in MAUD that can be used to fit lattice strains, resulting in diffraction peak shifts. Two are "stress models" that convert macroscopic stress tensor components to lattice strains and then are used to compute reflection positions, using the provided elastic properties of the material. The other two models fit lattice strain distributions and leave it up to the user to calculate stresses in the end.

In axial compression experiments in the DAC, the anvils impose both hydrostatic stresses (pressure) and differential stresses. The symmetric stress tensor $\tilde{A}_{ij}$ can be separated into hydrostatic $\tilde{A}_p$ and differential D_{ij} stress components such that:

$$\sigma_{ij} = \begin{bmatrix} \sigma_p & 0 & 0 \\ 0 & \sigma_p & 0 \\ 0 & 0 & \sigma_p \end{bmatrix} + \begin{bmatrix} -t/3 & 0 & 0 \\ 0 & -t/3 & 0 \\ 0 & 0 & 2t/3 \end{bmatrix} = \sigma_p + D_{ij} \qquad (1)$$

where t is the axial stress component and provides lower bounds for the yield strength of the material (Singh, 1993; Singh *et al*., 1998). Thus, during refinement of the stresses, the differential stresses should be constrained such that $\tilde{A}_{11} = \tilde{A}_{22}$ and $\tilde{A}_{33} = -2\tilde{A}_{11}$, where $\tilde{A}_{33}$ is the largest principal stress in the compression direction and is negative (corresponding to compression), according to the conventions in MAUD (component 33 of the stress is along the z axis of the sample or center of the pole figure). For the analysis described here, only differential stresses will be fit with the stress model. Hydrostatic stresses are accounted for by refining unit cell parameters, which in turn can be converted to pressure by utilizing an appropriate equation

of state (see below). The reason for treating these separately is that differential stresses will be calculated assuming a linear stress-strain relationship which is only applicable for small strains. The volume changes of the unit cell due to pressure effects are significantly larger than those due to differential stress, and it is best to use an equation of state which properly accounts for the nonlinearity of stress-strain dependence at larger compressions. On the other hand, for the analysis of the residual stresses, *e.g.*, in engineering materials, where stress tensor components values are often within a 0.5 GPa range, it is appropriate to keep initial lattice parameters fixed. One should then only fit either stress or strain values.

The four models in MAUD to fit stress-strain are: 1) a triaxial elastic stress (isotropic elastic constant, $\sin^2\psi$ method (Noyan and Cohen, 1987), 2) the moment pole stress (Matthies, 1996 and Matthies et al., 2001), 3) WSODF (Popa and Balzar, 2001), 4) the Radial Diffraction in the DAC (Singh, 1993 and Singh *et al*., 1998). Of these four models only the second and the fourth are appropriate for the type of analysis we want to do in this case[Luca please add a sentence to say why]. In the following we briefly describe how these two methods work.

Moment Pole Stress. This model requires the elastic tensor (C_{ij}), corrected for pressure (and temperature, if necessary), for the material of interest. It is the most sophisticated model of the four and calculates diffraction elastic constants for each diffraction peak of the material, taking preferred orientation into account using different micromechanical models similar to those used for calculating bulk polycrystal properties (*e.g.*, Voigt, Reuss, Hill, GEO). The only difference is that for calculation of diffraction elastic constants, crystal properties should be averaged, using “moments” of OD or pole figures (corresponding values weighted by sine or cosine values of certain angles).

Radial Diffraction in the DAC. This model is not a true “stress” model like the previous one. While the other models are more general and can be applied to more complicated deformation geometries, “Radial Diffraction in the DAC” can only be applied to axial compression. The main advantage of this model is that it allows the user to fit lattice strains for each peak separately whereas previous models imply that all the displacements of diffraction peaks correspond to one macrostress tensor, or they are restricted by crystal symmetry. The “Triaxial Stress Isotropic E” and “Moment Pole Stress” models may fail if plastic anisotropy of the material is high. In the case of ferropericlase some peaks exhibit much higher lattice strains than other peaks, and these two models may not be able to provide a satisfactory fit to the data.

This model fits a *Q(hkl)* factor to each diffraction peak based on peak displacement and the angle to the principal stress axis.

Correcting Young's Modulus and Poisson Ratio or C_{ij} to Pressure. As mentioned above, using the "Moment Pole Stress" or any stress fitting model (that requires the stiffness tensor or modulus), the elastic moduli must be corrected for pressure. Elastic moduli are pressure-dependent and often become larger as pressure increases or may display critical behavior near phase transitions. To correct elastic moduli for pressure, you will need an appropriate equation of state for your sample and a set of elastic moduli either calculated or experimentally determined for a range of pressures for your material. If your experiment is also at high temperature, you will need to correct for this as well. In addition, you must account for possible anisotropic thermal expansion of the sample.

The easiest way to correct the elastic moduli is to create a spreadsheet which uses an equation of state, such as a 3rd order Birch-Murnaghan equation of state, to calculate pressure from the fitted unit cell parameters. Next, plot each elastic coefficient (*e.g.*, C_{11}, C_{22}, C_{33}, C_{12} etc. or Young's modulus and Poisson's ratio) versus pressure. Once this is done, calculate a best fit line to each of the elastic constants and determine the equation describing the pressure dependence for each constant. This will allow you to extrapolate or interpolate elastic moduli to any reasonable pressure (for MgO see Marquardt et al. 2009). Often a linear extrapolation is sufficient. Now use the pressure calculated from your unit cell parameters to determine the appropriate value of the elastic moduli using the equations for your best fit lines. You may need to perform several iterations of this before the unit cell parameter and stress values stabilize. You have to calculate the pressure from the unit cell parameter, correct the elastic moduli to the pressure, input the corrected elastic moduli, and run the refinement. After doing this you may notice that the unit cell parameter has changed. If so you will need to repeat the previous procedure until the unit cell parameter (and the corresponding pressure value) converge to a stable value.

Using the "Radial Diffraction in the DAC" model we can avoid such an iterative procedure and get directly the differential stress and calculate the pressure from the equation of state.

D. Refinement

In this case the refinement is quite complex involving strong texture and high stresses with limited data. We need to guide the refinement and accurately choose the parameters to refine. We try as much as possible to avoid refining unnecessary parameters. In summary the refinement involves the following steps (see also Appendix 2):

- *Beam intensity*. We refine only beam intensity as we use an interpolated background.
- *Cell parameters*. Ferropericlase is cubic, so we need to refine only the unit cell parameter *a*.
- *Texture.* As seen in the Figure 10 the texture is fairly sharp, thus we refine the texture early. With the E-WIMV method we obtaine a first OD without any sample symmetry to check and validate our hypothesis of imposing an axial symmetry (Figure 10a). Once we verify that the texture and sample orientation is compatible with axial symmetry, we impose a "fiber" sample symmetry (Fig. 10b). This greatly improves the effective pole figure coverage.
- *Crystallite size and r.m.s. microstrain*. Here we assume isotropic crystallite size and microstrain which corresponds to two parameters. As mentioned earlier, with the coarse-grained LaB_6 standard, it was difficult to refine an accurate instrument peak shape.
- *Stress models*. For "Moment pole stress" we start with the elastic tensor values for ferropericlase at atmospheric pressure with $C_{11} = C_{22} = C_{33} = 279.5$ GPa, $C_{12} = C_{13} = C_{23} = 102.2$ GPa, $C_{44} = C_{55} = C_{66} = 142$ GPa, with all others equal to zero (Marquardt *et al*., 2009) and we refine only the σ_{11} macrostress value. As an alternative for the "Radial Diffraction in the DAC" model we refine *Q(hkl)* factors of each diffraction peak in the refinement range 4 parameters).
- *Beam center*. If your reflection positions are not fitting well with the stress model and you still observe variations of peak position with angle η, refine the detector center errors (2 parameters, *x* and *y*), since it may have changed during DAC positioning. In our case it was not necessary.
- *Tilt of the DAC cell.* If there is evidence that the compression direction is tilted (not in this case), then we need to correct for this. In the "Radial Diffraction in the DAC" model, it is accomplished by refining the "Alpha" and "Beta" angles for a better fit. In the other

stress based models, the only option is to refine the sample orientation angles that define the coordinate system.

- *Heterogeneities of strain in the DAC cell.* In the "Plot 2D" display you may observe asymmetry in the texture between the lower and the upper half of the measured spectra display, while refined spectra demonstrate perfect symmetry. This may be due to heterogeneities of the sample in the DAC, *e.g.* some grains in the periphery of the cell are subjected to lower pressures and deviatoric stress. To accommodate this, one can use for the last refinement cycle only one half of the diffraction image. However if only half the Debeye ring is used one should be sure to fix beam center and tilt parameters. Since axial symmetry of texture and stress state is imposed, the entire diffraction image is not needed to derive a reasonably accurate OD.

Final results. At the end of the analysis the refined cell parameter is 3.9866(1) Å and the corresponding volume is H63.36 Å^3. For radial diffraction the lattice parameter represents the strain resulting from the hydrostatic (pressure) component of the stress tensor. The derived pressure is H39.6 GPa and the final elastic tensor is $C_{11} = C_{22} = C_{33}$ H624.4 GPa, $C_{12} = C_{13} = C_{23}$ H171.1 GPa, $C_{44} = C_{55} = C_{66}$ H175.3 GPa; the differential macrostress σ_{11} component is H 1.80(1) GPa. To calculate the equivalent *t* value in equation (1) we multiply by 3 this value to obtain 5.4 GPa.

In this analysis we have been mainly concerned with preferred orientation which, for axially symmetric textures, is conveniently displayed as inverse pole figures that represent the probability of the fiber axis relative to crystal coordinates. Figure 10c is the inverse pole figure of the compression direction plotted in MAUD and Figure 10d the corresponding inverse pole figure after processing with BEARTEX. The texture is moderate, with a pole density maximum of H2.65 multiples of a random distribution, located close to 001 (Fig. 10d), as previously observed (*e.g.*, Merkel *et al*., 2002; Kunz *et al*., 2009, Lin *et al*., 2009, Kaercher et al., 2012).

IV. CONCLUSIONS

Synchrotron X-rays provide a powerful method for quantitative texture analysis of materials. Depending on sample size, beam size and wavelength, small (< 100 μm^3) to large volumes (> 200 mm^3) can be analyzed, and different sample equipment can be used to impose different conditions on the sample (*e.g.*, high pressure, high temperature, anisotropic stress).

Compared to neutron diffraction, electron backscatter diffraction or pole-figure goniometry, data acquisition is fast, but data analysis is non-trivial. For complex polyphase materials (such as the shale sample) a careful manual procedure is necessary. Further complications arise for high pressure experiments, where anisotropic stresses need to be accounted for. MAUD incorporates a set of methods able to account for preferred orientations, anisotropic stresses and microstructural characteristics of material. Here we provided only a brief overview of these and simplified step-by-step procedures that give general directions for the analysis, while highlighting some possible complications. Knowledge of the instrument, sample, and experimental setup is necessary to adjust these procedures to each specific case and obtain convincing results.

Acknowledgements

This project was supported by NSF (EAR-0836402) and DOE (DE-FG02-05ER15637). We greatly appreciate access to beamline 11-ID-C at APS of Argonne National Laboratory and help from Chris Benmore and Yang Ren, as well as access to beamline 12.2.2. at ALS of Lawrence Berkeley Laboratory and help from Jason Knight. The tutorial was developed as part of a workshop at the Advanced Light Source in fall 2012, supported by CDAC, APS (BESSRC), NSF-COMPRES, ALS and STONE-LANL. RV appreciates support of AYSS JINR (12-401-01). We appreciate input from many MAUD users, especially Juan Gomez-Barreiro, the Editor Brian Toby and three reviewers that helped us improve the manuscript.

References

Bish, D.L., and Von Dreele, R.B. (**1989**). "Rietveld refinement of non-hydrogen atomic positions in kaolinite," Clays and Clay Minerals **37**, 289-296.

Grässlin, J., McCusker, L.B., Baerlocher, C., Gozzo, F., Schmitt, B., and Lutterotti, L. (**2013**). "Advances in exploiting preferred orientation in the structure analysis of polycrystalline materials," Journal of Applied Crystallography **46**, 173-180.

Gražulis, S., Chateigner, D., Downs, R.T., Yokochi, A.F.T., Quirós, M., Lutterotti, L., Manakova, E., Butkus, J., Moeck, P., and Le Bail, A. (**2009**). "Crystallography Open Database – an open access collection of crystal structures," Journal of Applied Crystallography **42**, 726-729.

Gualtieri, A.F. (**2000**). "Accuracy of XRPD QPA using the combined Rietveld-RIR method," Journal of Applied Crystallography **33**, 267-278.

Hammersley, A.P. (**1998**) Fit2D: V99.129 Reference Manual Version 3.1. Internal Report ESRF – 98 – HA01.

Hornby, B.E. **(1998)**. "Experimental laboratory determination of the dynamic elastic properties of wet, drained shales," Journal of Geophysical Research **103** (B12), 29945-29964.

Kaercher, P., Speziale, S., Miyagi, L., Kanitpanyacharoen, W., and Wenk, H.-R. **(2012)**. "Crystallographic preferred orientation in wüstite (FeO) through the cubic-to-rhombohedral phase transition," Physics and Chemistry of Minerals **39**, 613-626.

Kanitpanyacharoen, W., Merkel, S., Miyagi, L., Kaercher, P., Tomé, C.N., Wang, Y., and Wenk, H.-R. **(2012b)**. "Significance of mechanical twinning in hexagonal metals at high pressure," Acta Materialia **60**, 430-442.

Kanitpanyacharoen, W., Wenk, H.-R., Kets, F., Lehr, B.C., and Wirth, R. **(2011)**. "Texture and anisotropy analysis of Qusaiba shales," Geophysical Prospecting **59**, 536-556.

Kanitpanyacharoen, W., Kets, F.B., Wenk, H.-R., and Wirth, R. **(2012a)**. "Mineral preferred orientation and microstructure in the Posidonia Shale in relation to different degrees of thermal maturity," Clays and Clay Minerals **60**, 315-329.

Kunz, M., Caldwell, W.A., Miyagi, L., and Wenk, H.-R. **(2007)**. "In situ laser heating and radial synchrotron x-ray diffraction in a diamond anvil cell," Review of Scientific Instruments **78**, 063907, 1-6.

Le Bail, A., Duroy, H., and Fourquet, J.L. (**1988**). "Ab-initio structure determination of $LiSbWO_6$ by X-ray powder diffraction," Materials Research Bulletin **23**, 447-452.

Lin J.-F., Wenk H.-R., Voltolini, M., Speziale S., Shu J., and Duffy T. **(2009)**. "Deformation of lower mantle ferropericlase (Mg,Fe)O across the electronic spin transition," Phys. Chem. Minerals **37**, 585-592.

Lutterotti, L. (**2005**). "Quantitative Rietveld analysis in batch mode with Maud, and new features in Maud 2.037," Newsletter of the Commission on Powder Diffraction, IUCr, **32**, 53-55.

Lutterotti, L., Chateigner, D., Ferrari, S., Ricote, J. **(2004)** "Texture, residual stress and structural analysis of thin films using a combined X-ray analysis," Thin Solid Films **450**, 34-41.

Lutterotti, L., Bortolotti, M., Ischia, G., Lonardelli, I., and Wenk, H.-R. (**2007**). "Rietveld texture analysis from diffraction images," Z. Kristallographie suppl. **26**, 125-130.

Lutterotti, L., Matthies, S., Wenk, H.-R., Schultz, A.S., and Richardson, J.W. (**1997**). "Combined texture and structure analysis of deformed limestone from time-of-flight neutron diffraction spectra," Journal of Applied Physics **81**, 594-600.

Lutterotti, L., Voltolini, M., Wenk, H.-R., Bandyopadhyay, K., and Vanorio, T. (**2010**). "Texture analysis of turbostratically disordered Ca-montmorillonite," American Mineralogist **95**, 98-103.

Lutterotti, L., Vasin, R.N. and Wenk, H.-R. **(2013)**. "Rietveld texture analysis from synchrotron diffraction images: I. Basic analysis," Powder Diffraction (in press).

Marquardt, H., Speziale, S., Reichmann, H.J., Frost, D.J., and Schilling, F. R. **(2009)**. "Single-crystal elasticity of $(Mg_{0.9}Fe_{0.1})O$ to 81 GPa," Earth and Planetary Science Letters **287**, 345-352.

Matthies, S. (**1996**). "Moment pole figures in residual stress analysis," Textures Microstructures **25**, 229-236.

Matthies, S., and Wenk, H.-R **(2009)**. "Transformations for monoclinic crystal symmetry in texture analysis," Journal of Applied Crystallography **42**, 564-571.

Matthies, S., Priesmeyer, H.G., and Daymond, M.R. **(2001)**. "On the diffractive determination of single-crystal elastic constants using polycrystalline samples," Journal of Applied Crystallography **34**, 585-601.

Matthies, S., Vinel, G.W., and Helming, K. (**1987**). "*Standard Distributions in Texture Analysis,*" Akademie-Verlag, Berlin FRG.

Merkel, S., Wenk, H.-R., Shu, J., Shen, G., Gillet, P., Mao, H.-K., and Hemley, R.J. **(2002)**. "Deformation of polycrystalline MgO at pressures of the lower mantle," Journal of Geophysical Research **107** doi:10.1029/2001JB000920, 1-17.

Merkel, S. **(2006)**. "X-ray diffraction evaluation of stress in high pressure deformation experiments," Journal of Physics: Condensed Matter **18**, S949-962.

Miyagi, L., Kanitpanyacharoen, W., Kaercher, P., Lee, K.K.M., and Wenk, H.-R. **(2010)**. "Slip systems in $MgSiO_3$ post-perovskite: Implications for D'' anisotropy," Science **329**, 1639-1641.

Miyagi, L., Kunz, M., Knight, J., Nasiatka, J., Voltolini, M., and Wenk, H.-R. **(2008)**. "*In situ* phase transformation and deformation of iron at high pressure and temperature," Journal of Applied Physics **104**, 103510, 1-9.

Miyagi. L., Kanitpanyacharoen. W., Kaercher. P., Knight. J., Raju. V., Zepeda. E., Wenk. H.R., and Williams. Q. **(2013)**. "Combined resistive and laser heating in diamond anvil high pressure experiments". Rev. Sci. Instr. (in press).

Noyan, I.C., and Cohen, J.B. (**1987**). "*Residual stress: measurement by diffraction and interpretation,*" Springer Verlag, Berlin.

Plançon A., Tsipurski S.I., and Drits V.A. **(1985)**. "Calculation of intensity distribution in the case of oblique texture electron diffraction," Journal of Applied Crystallography **18**, 191-196.

Popa, N.C., (**1992**). "Texture in Rietveld Refinement," Journal of Applied Crystallography **25**, 611-616.

Popa, N.C., and Balzar, D. (**2001**). "Elastic strain and stress determination by Rietveld refinement: generalized treatment for textured polycrystals for all Laue classes," Journal of Applied Crystallography **34**, 187-195.

Singh, A.K. **(1993)**. "The lattice strains in a specimen (cubic system) compressed nonhydrostatically in an opposed anvil device," Journal of Applied Physics 73, 4278-4286.

Singh, A.K., Mao, H.-K., Shu, J., and Hemley, R.J. **(1998)**. "Estimation of single-crystal elastic moduli from polycrystalline X-ray diffraction at high pressure: application to FeO and iron," Physical Review Letters **80**, 2157-2160.

Sonneveld, E.J., and Visser, J.W. (**1975**). "Automatic Collection of Powder Data from Photographs," Journal of Applied Crystallography **8**, 1-7.

Ufer, K., Roth, G., Kleeberg, R., Stanjek, H., Dohrmann, R., and Bergmann, J. **(2004)**. "Description of X-ray powder pattern of turbostratically disordered layer structures with a Rietveld compatible approach," Zeitschrift für Kristallographie **219**, 519-527.

Vasin, R., Wenk, H.-R., Kanitpanyacharoen, W., Matthies, S., and Wirth, R. **(2013)**. "Anisotropy of Kimmeridge shale," Journal of Geophysical Research **118**, 1-26, doi:10.1002/jgrb.50259.

Wenk, H.-R., Lonardelli, I., Merkel, S., Miyagi, L., Pehl, J., Speziale, S., and Tommaseo, C.E. **(2006)**. "Deformation textures produced in diamond anvil experiments, analyzed in radial diffraction geometry," Journal of Physics: Condensed Matter **18**, S933-947.

Wenk, H.-R., Ischia, G., Nishiyama, N., Wang, Y., and Uchida, T. **(2005)**. "Texture development and deformation mechanisms in ringwoodite," Physics of the Earth and Planetary Interiors **152**, 191-199.

Wenk, H.-R., Matthies, S., Donovan, J., and Chateigner, D. (**1998**). "BEARTEX: a Windows-based program system for quantitative texture analysis," Journal of Applied Crystallography **31**, 262-269.

Wenk, H.-R., Voltolini, M., Kern, H., Popp, T., and Mazurek, M. **(2008)**. "Anisotropy in shale from Mont Terri," The Leading Edge **27**, 742-748.

Wenk, H.R., Kaercher, P., Kanitpanyacharoen, W., Zepeda-Alacon, E., and Wang, Y. **(2013)**. "Orientation relations during the α–ω phase transition of zirconium - *in situ* texture observations at high pressure and temperature". Physics Review Letters 111, 195701, doi:10.1103/PhysRevLett.111.195701.

Tables

Table I Phase volume and weight fractions of minerals in shale (in %), with and without imposed axial symmetry of texture.

	Vol. Axial	Wgt. Axial	Vol. No symm.	Wgt. No symm.	Vol. Full range	Wgt. Full range
Kaolinite	9.9(2)	9.1(2)	8.7(1)	8.1(1)	11.8(1)	10.8(1)
Illite-mica	29.8(5)	29.7(5)	32.5(2)	32.9(2)	27.0(1)	27.0(1)
Illite-smectite	24.5(7)	22.8(6)	31.8(2)	29.7(2)	32.6(2)	31.7(2)
Quartz	30.6(5)	29.1(5)	22.9(1)	21.9(1)	24.7(1)	23.5(1)
Pyrite	5.2(5)	9.3(8)	4.1(1)	7.4(1)	3.9(1)	7.0(1)

Table II Texture information for phyllosilicates in shale after processing in BEARTEX, pole densities in m.r.d.

	Max axial	Min axial	Max No symm.	Min No symm	Max full range	Min full range
Kaolinite 001	6.84	0.22	5.14	0.31	4.44	0.15
Illite-mica 100	8.50	0.12	7.78	0.25	9.73	0.21
Illite-smectite 100	3.83	0.39	3.70	0.30	3.22	0.32

Table III Texture information for magnesiowuestite at 39.6 GPa; pole densities of different pole figures and inverse pole figure (IPF) in m.r.d.

	Max	Min	Max No symm.	Min No symm
100	2.65 2.64 (2.74)	0.72 0.67 (0.73)	2.57	0.55
110	1.24 1.12 (1.26)	0.87 0.75 (0.86)	1.47	0.59
111	1.31 1.12 (1.26)	0.54 0.51 (0.53)	1.55	0.44

Comment [L1]: I wonder if it wouldn't be more useful to put in the values from MAUD since some people following the tutorial may not have beartex, and it is quicker just to check in MAUD

IPF	2.65 3.19 (2.74)	0.54 0.51 (0.53)		

Figure Captions

Figure 1. (a) Slab of shale embedded in epoxy and mounted on a pin. (b) Pole figure coverage with a single image, bedding plane normal is at B. When cylindrical symmetry is imposed, each point covers a circle around B on the pole figure (c) Coverage with seven images recorded at different sample tilts ω.

Figure 2. 2D synchrotron diffraction images. (a) Kimmeridge shale with many phases, some with strong preferred orientation. (b) LaB_6 standard, rather coarse-grained and with some impurities. (c) Radial diffraction DAC experiment on ferropericlase at 39.6 GPa. Arrow points to a diffraction spot from diamond.

Figure 3. Stack of diffraction spectra for Kimmeridge shale, $\omega = 0^{o}$ tilt image. Experimental data at bottom and Rietveld fit on top. Some diffraction lines are labeled.

Figure 4. Two diffraction spectra of Kimmeridge shale with scattering lattice planes parallel to bedding plane on top and perpendicular to it at bottom. Crosses are measured data and line is Rietveld fit. Below the spectra is a list of contributing phases and their corresponding diffraction peak positions are marked with ticks.

Figure 5. Pole figures of basal planes of kaolinite, illite-mica and illite-smectite for Kimmeridge shale. (a) Derived from a single image, imposing fiber symmetry. (b) Result for 7 images without imposing symmetry. The corresponding pole figure coverage is shown in Fig. 1c. Equal area projection on the bedding plane, contours in multiples of a random distribution.

Figure 6. Cumulative plot for all patterns of the ω=0 image at the end of refinement cycles with 7 images. Dots are experimental data and line is Rietveld fit.

Figure 7. Pole figures 100 of kaolinite and 001 of illite-mica and illite-smectite for Kimmeridge shale without imposing sample symmetry. The corresponding pole figure coverage is shown in Fig. 1c. Equal area projection on the bedding plane, contours in multiples of a random distribution.

Figure 8. (a,b) Schematic sketch illustrating the geometry of deformation experiments in a diamond anvil cell in radial diffraction geometry. (c) Actual diamond culets compressing a sample contained by a gasket. (d) Pole figure coverage for the magnesiowuestite DAC experiment. A gap is visible where one pattern is disabled because of the beam stop masking.

Figure 9. Measured (bottom) and calculated (top) diffraction spectra for ferropericlase; (a) at the beginning of the refinement. Lattice parameters are wrong and there is no texture or anisotropic stress in the model. Also note the black diffraction spot from diamond. (b) At the end of the refinement there is an excellent match in position, width and intensity. The compression direction is indicated by the black arrow in (a) (larger 2¸ angle corresponding to smaller *d*-spacing).

Figure 10. Texture information for ferropericlase at 39.6 GPa represented as pole figures (a-b) and inverse pole figures (c-d). (a) Pole figures without imposing sample symmetry. (b) Pole figures imposing fiber symmetry. (c) Inverse pole figure of the compression direction plotted by MAUD. (d) Inverse pole figure after processing data in BEARTEX. Equal area projection, contours in multiples of a random distribution.

Figures Part II

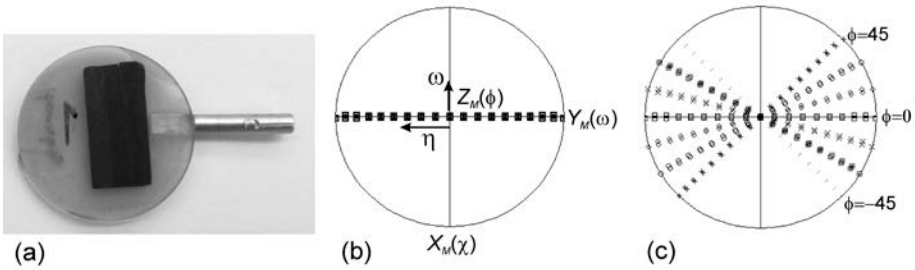

Figure 1. (a) Slab of shale embedded in epoxy and mounted on a pin. (b) Pole figure coverage with a single image, bedding plane normal is in the center of the pole figure. When fiber symmetry is imposed, each point covers a circle. (c) Coverage with seven images recorded at different sample rotations ϕ around the Z axis.

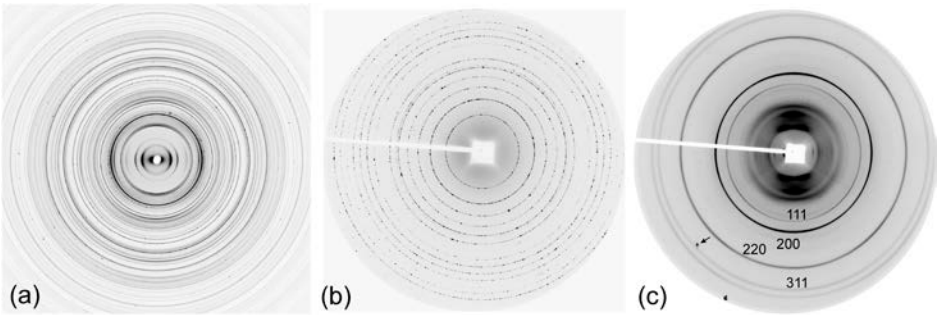

Figure 2. 2D synchrotron diffraction images. (a) Kimmeridge shale with many phases, some with strong preferred orientation. (b) LaB_6 standard used for the DAC experiment, rather coarse-grained and with some impurities. (c) Radial diffraction DAC experiment on magnesiowuestite. Arrow points to a diffraction spot from diamond. The compression direction is vertical.

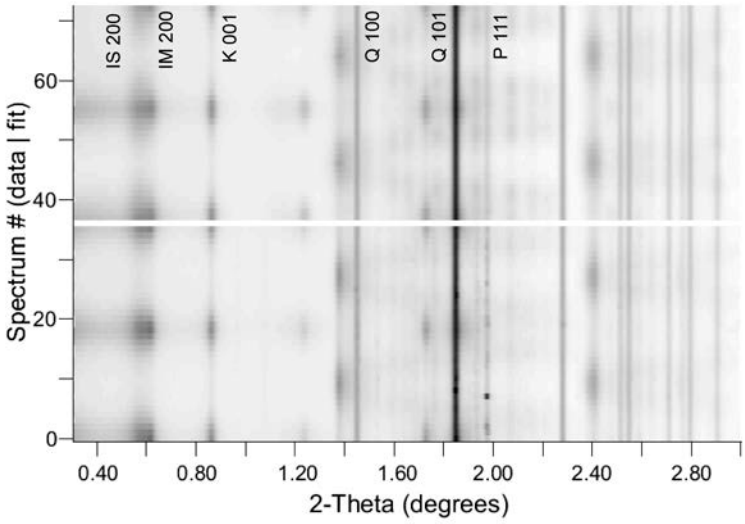

Figure 3. Stack of diffraction spectra for Kimmeridge shale, $\phi = 0^{o}$ tilt image. Experimental data at bottom and Rietveld fit on top. Some diffraction for lines for illite-smectite (IS), illite-mica (IM), kaolinite (K), quartz (Q) and pyrite (P) are labeled.

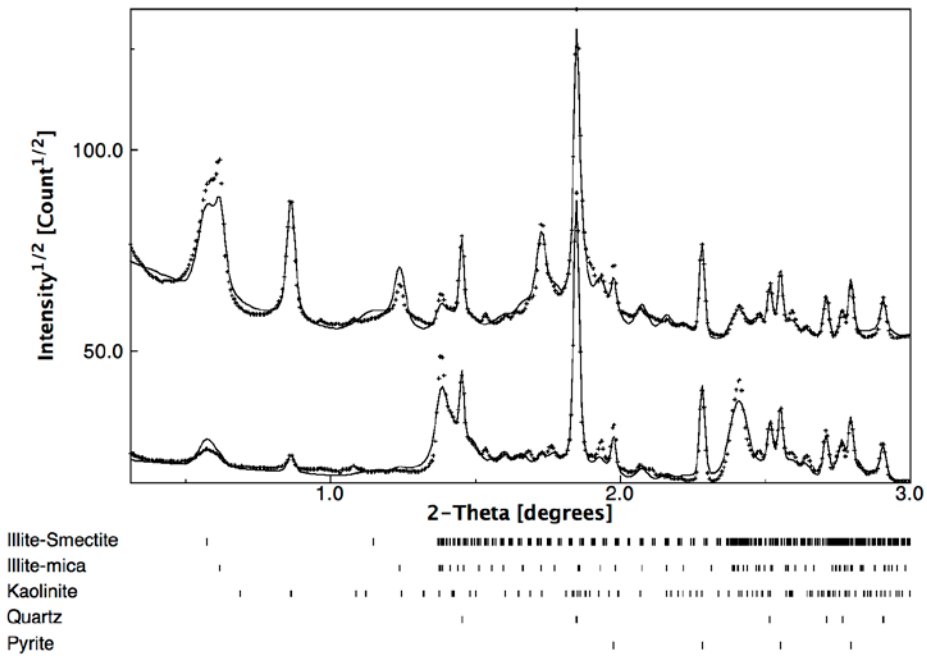

Figure 4. Two diffraction spectra of Kimmeridge shale with scattering lattice planes parallel to bedding plane on top and perpendicular to it at bottom. Crosses are measured data and line is Rietveld fit. Below the spectra is a list of contributing phases and their corresponding diffraction peak positions are marked with ticks.

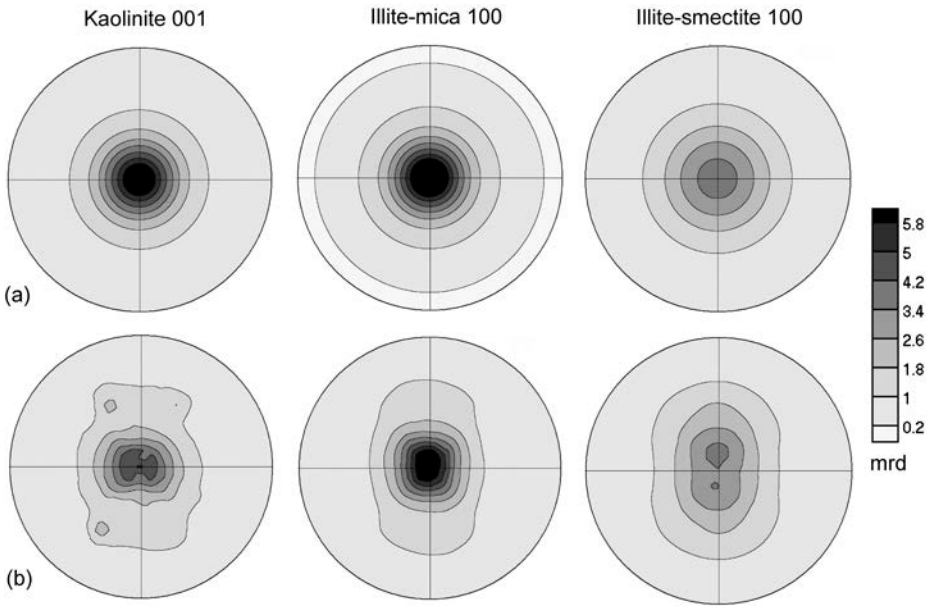

Figure 5. Pole figures of basal planes of kaolinite, illite-mica and illite-smectite for Kimmeridge shale after exporting the orientation distributions from MAUD and processing them with BEARTEX. (a) Derived from a single image, imposing fiber symmetry. (b) Result for 7 images without imposing symmetry. The corresponding pole figure coverage is shown in Fig. 1c. Equal area projection on the bedding plane, contours in multiples of a random distribution.

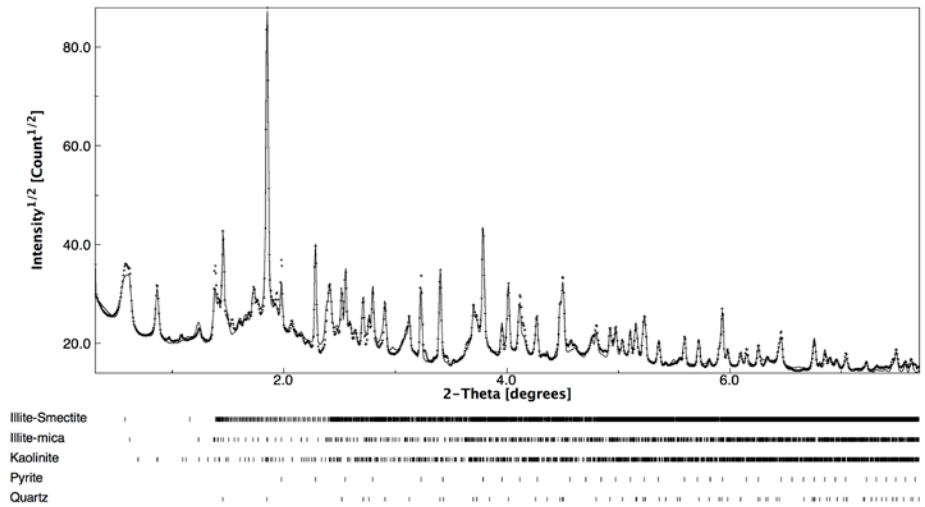

Figure 6. Cumulative plot for all patterns of the ϕ=0 image at the end of refinement cycles with 7 images. Dots are experimental data and line is Rietveld fit.

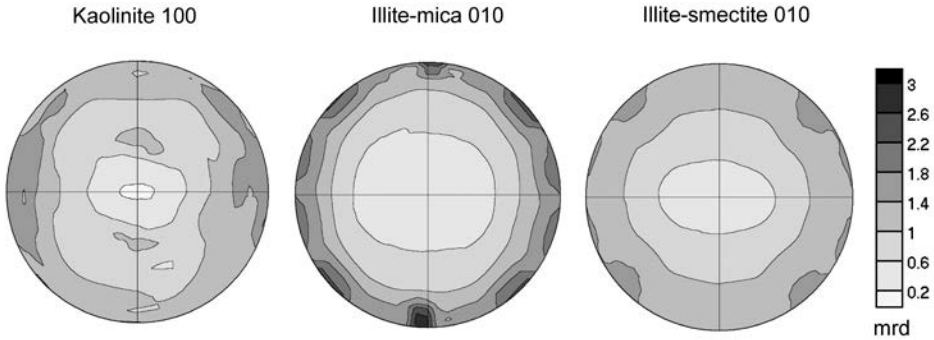

Figure 7. Pole figures 100 of kaolinite and 010 of illite-mica and illite-smectite for Kimmeridge shale without imposing sample symmetry. The corresponding pole figure coverage is shown in Fig. 1c. Equal area projection on the bedding plane, contours in multiples of a random distribution.

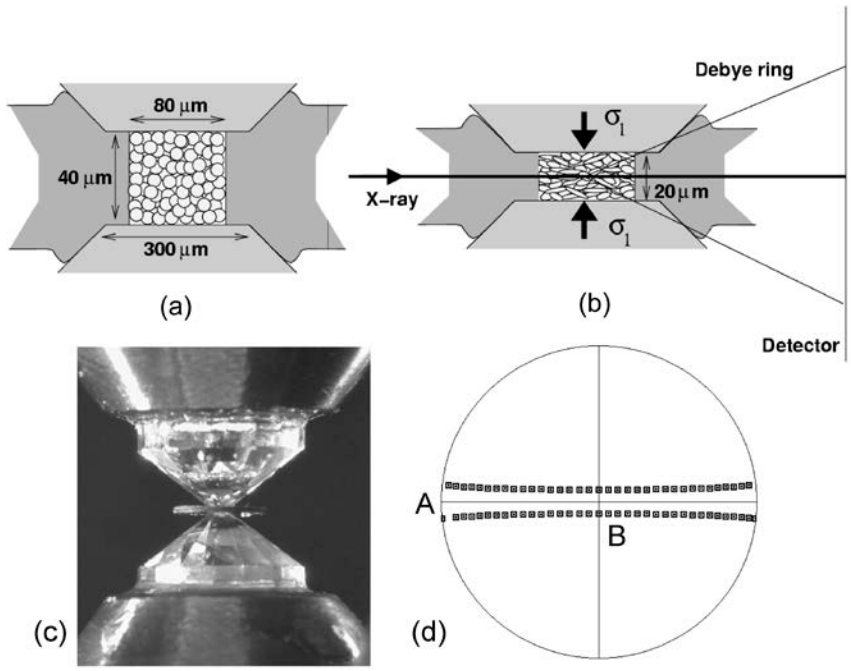

Figure 8. (a,b) Schematic sketch illustrating the geometry of deformation experiments in a diamond anvil cell in radial diffraction geometry. (c) Actual diamond culets compressing a sample contained by a gasket. (d) Pole figure coverage for the magnesiowuestite DAC experiment. A gap is visible where one pattern is disabled because of the beam stop masking.

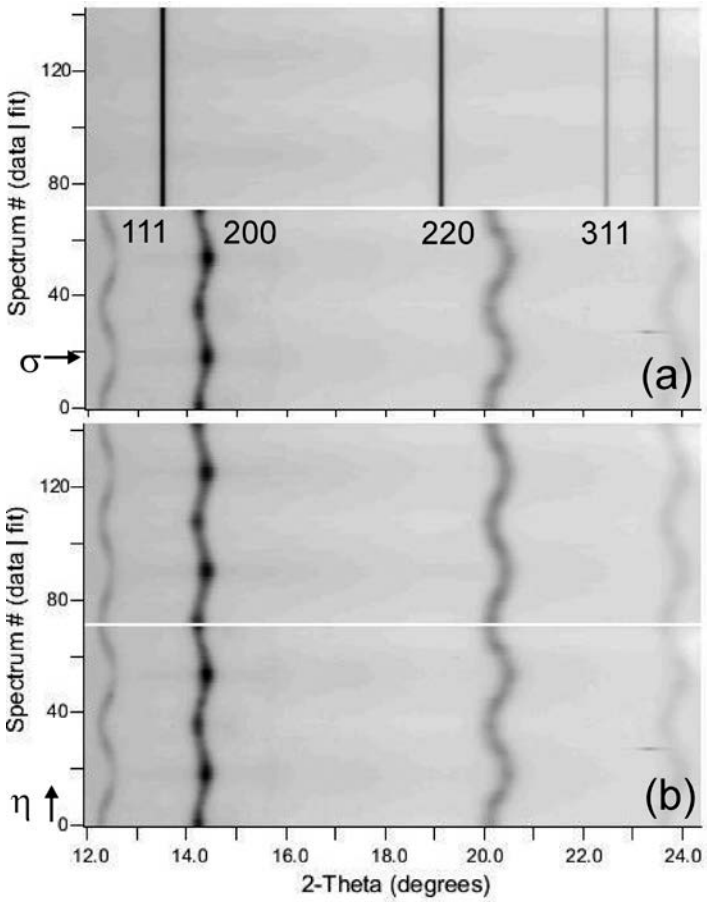

Figure 9. Measured (bottom) and calculated (top) diffraction spectra for magnesiowuestite; (a) at the beginning of the refinement. Lattice parameters are wrong and there is no texture or anisotropic stress in the model. Also note the black diffraction spot from diamond at 2θ=23.5. (b) At the end of the refinement there is an excellent match in position, width and intensity. The compression direction σ is indicated by the black arrow in (a) (larger 2¸ angle corresponding to smaller *d*-spacing).

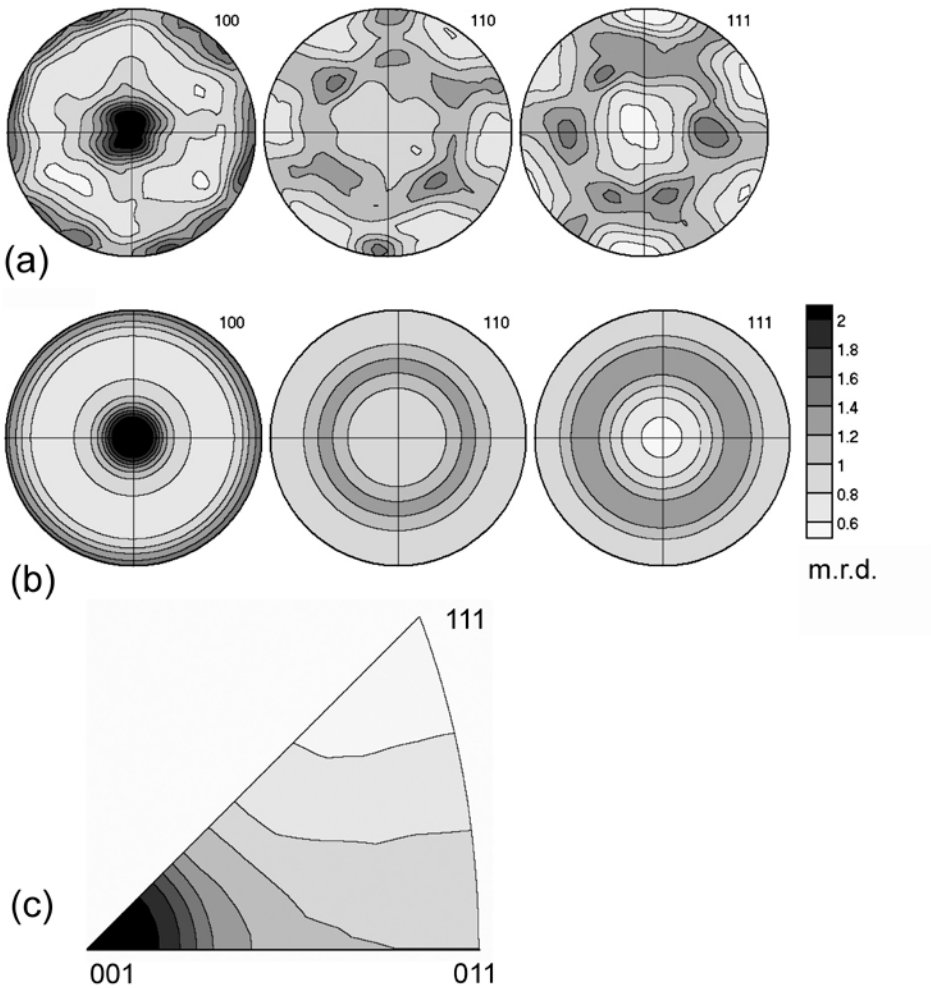

Figure 10. Texture information for magnesiowuestite at 39.6 GPa represented as pole figures (a-b) and inverse pole figures (c-d). (a) Pole figures without imposing sample symmetry. (b) Pole figures imposing fiber symmetry. (c) Inverse pole figure of the compression direction plotted by MAUD. (d) Inverse pole figure after processing data in BEARTEX. Equal area projection, contours in multiples of a random distribution.

Appendix

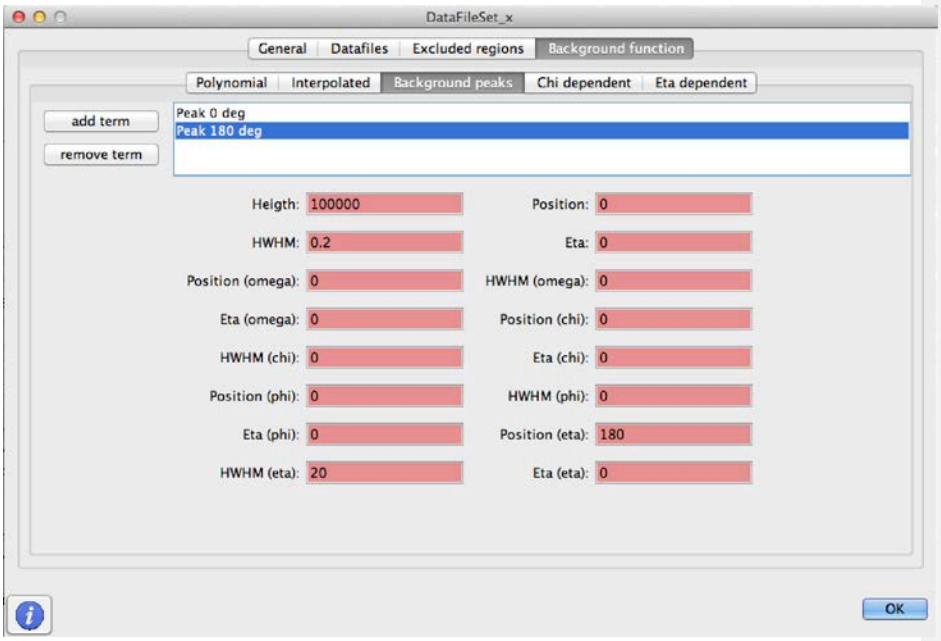

Figure A1-1. Window in MAUD to define background peaks.

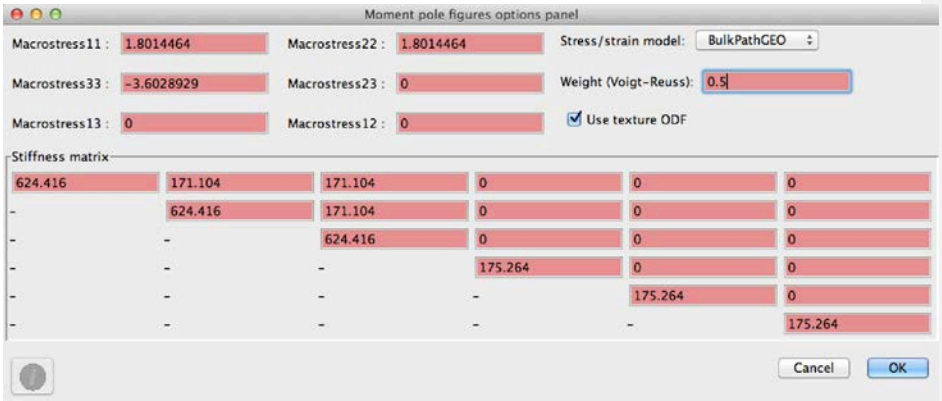

Figure A2-1. MAUD window for moment pole figures option to use as a stress/strain model.

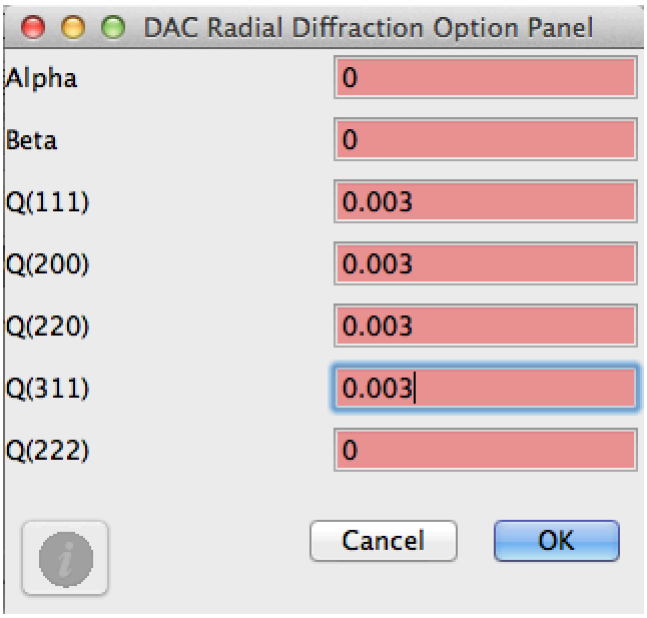

Figure A2-2. MAUD radial diffraction option panel for stress-strain refinement.